Tunneling of hybridized pairs of electrons through a one-dimensional channel

Godfrey Gumbs, Danhong Huang, Julie Hon, M. Pepper & Sanjeev Kumar

Published online: 28 May 2017.

Submit your article to this journal ↗

Article views: 59

View related articles ↗

View Crossmark data ↗

Taylor & Francis
Taylor & Francis Group

REVIEW ARTICLE

Tunneling of hybridized pairs of electrons through a one-dimensional channel

Godfrey Gumbs[a,b] , Danhong Huang[c], Julie Hon[a], M. Pepper[d,e] and Sanjeev Kumar[d,e]

[a]Department of Physics and Astronomy, Hunter College of the City University of New York, New York, NY, USA; [b]Donostia International Physics Center (DIPC), San Sebastian, Spain; [c]Air Force Research Laboratory, Space Vehicles Directorate, Kirtland Air Force Base, Albuquerque, NM, USA; [d]London Centre for Nanotechnology, London, UK; [e]Department of Electronic and Electrical Engineering, University College London, London, UK

ABSTRACT

Recently, the electron transport through a quasi-one dimensional (quasi-1D) electron gas was investigated experimentally as a function of the confining potential. We present a physical model for quantum ballistic transport of electrons through a short conduction channel, and investigate the role played by the Coulomb interaction in modifying the energy levels of two-electron states at low temperatures as the width of the channel is increased. In this regime, the effect of the Coulomb interaction on the two-electron states has been shown to lead to four split energy levels, including two anticrossings and two crossing-level states. Due to the interplay between the anticrossing and crossing of the energy levels, the ground state for the two-electron model switches from one anticrossing state for strong confinement to a crossing state for intermediate confinement as the channel width is first increased, and then returned to its original anticrossing state. This switching behavior is related to the triplet spin degeneracy as well as the Coulomb repulsion and reflected in the ballistic conductance. Here, many-body effects can still affect electron occupations in the calculation of quantum ballistic conductance although it cannot vary the center-of-mass velocity.
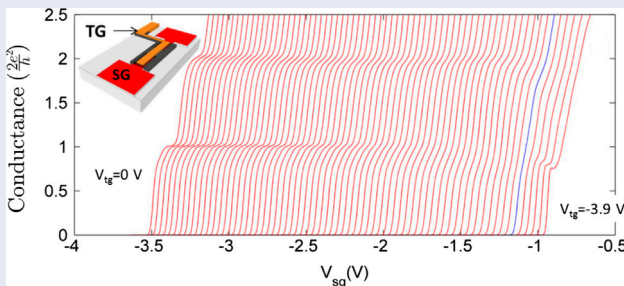
CONTACT   Godfrey Gumbs   ggumbs@hunter.cuny.edu

1. Introduction

In this paper, we review the importance of many-body effects on the ballistic electron transport in a quasi-one-dimensional (1D) electron gas with varied confinement potential. This area of research has been receiving a considerable amount of attention in recent times ever since it was discovered that for a range of electron distribution and potential strength, the ground state of a 1D quantum wire splits into two rows with a Wigner lattice beginning to form. It was also demonstrated that when a perpendicular magnetic field is applied, a double-row electron formation may change completely into a single row due to an enhanced confinement potential. Furthermore, it has been verified experimentally that weak confinement, in competition with the electron–electron interaction, causes the electron level occupation to reorder so that the ground state, conforming to the standard or common type, passes through the excited levels. The data in Ref. [1] show that the energy levels may be controlled by exploiting their separate geometric dependence on confinement and electron density. This means that in simulating the electron transport data, many-body effects must be considered.

It has been well known that electrostatic potential confinement of a two-dimensional electron gas (2DEG) used to create a quasi-1D wire [2] gives rise to quantization of the conductance [3,4] in integer multiples of $2\,e^2/h$ which is not affected by a weak electron–electron interaction [5]. The long-range Coulomb interaction between electrons becomes relatively important at low electron densities resulting in the formation of a 1D Wigner crystal [2,6,7]. But, the role played by the Coulomb repulsion between electrons is also made greater until it overcomes the confinement potential, as the density is increased, at which point the ground state and one of the excited states are interchanged [8] which may result in hybridization and anticrossing. In Refs. [1,9], conductance measurements were reported for weakly confined quantum wires in a 2DEG and determined by the boundaries of top split-gates.

Experiment has shown that making the confinement potential less effective results in the appearance of two rows, accompanied by a sudden change in conductance G from zero to $4\,e^2/h$. This behavior may be attributed to the possibility that there was no coupling between these two rows so that each row contributes independently and additively. Another way to account for this is to say that their energy eigenstates become hybridized and the resulting state causes a breakdown of the single-particle picture when the Coulomb interaction becomes important. Recent investigations have confirmed that there exists a Coulomb interaction between the rows resulting in this anomalous jump in the conductance [10].

The devices used in Refs. [1] and [9] were fabricated using electron beam lithography on 300 nm deep GaAs/AlGaAs heterostructures. Typically, the sample consisted of split gates, $\sim 0.4\,\mu$m long and $0.7 \sim 1.0\,\mu$m wide, and a top gate of width $\sim 1.0\,\mu$m defined above the split gates, separated by a 200 nm layer

of cross-linked polymethyl methacrylate. After partial illumination, the carrier density and mobility were estimated to be $\sim 1.5 \times 10^{11}\,\mathrm{cm}^{-2}$ and $\sim 1.3 \sim 3 \times 10^6\,\mathrm{cm}^2/\mathrm{Vs}$, respectively. The two-terminal conductance, $G = \mathrm{d}I/\mathrm{d}V$, was measured at 70 mK, using a 77 Hz voltage of $10\,\mu\mathrm{V}$. Previously, the conductance through two laterally aligned but uncoupled parallel wires formed by surface gates have been shown to be the sum of the conductances of each individual wire, resulting in plateaus at multiples of $4\,e^2/h$, [11,12] indicating that hybridization of states within a wire is a many-body effect but not a single-particle one. Two side-by-side wires with very small inter-wire separation have lent support for the theory, i.e. there exists a coupling between the parallel wires [13,14]. When this coupling between wires becomes strong, the electron wave functions hybridize, forming bonding and antibonding states, which manifest as anticrossings in the 1D energy subbands. Our model calculations [15] further confirm that the minimum energy gap between the states occurs at the point of anticrossing but is not given by the energy difference between the symmetric and antisymmetric states.

In Figure 1, we present a schematic illustration of a device used in the experiments carried out in Refs. [1,9], showing a pair of split gates and a top gate which adjust the confinement potential and carrier density by choosing their voltages suitably. Figure 1 also shows typical conductance features obtained with the device used in Ref. [1] as a function of the split-gate voltage, V_{sg}, for fixed top-gate voltage, V_{tg}. The traces for strong confinement are on the left-hand side, whereas those for weak confinement are on the right. When the confinement is weak, the $2\,e^2/h$ step may be lost and the $4\,e^2/h$ appears as the lowest plateau [1]. But, as the confinement is reduced further, the $2\,e^2/h$ plateau is found to be restored.

With regard to the interpretation that the carriers separate into two rows, the observed emergence of the crossing or anticrossing of energy levels needs explanation, preferably with the use of a quantum-mechanical theory. This may be verified by calculations of the kinetic, direct Coulomb, and exchange energies of electrons in wires with intermediate widths as well as for two extreme limits of very narrow and wide wires. In fact, we have recently demonstrated that these cases may be tracked down to the physical mechanism responsible for switching of the ground state as the wire width is varied from one value to another [15]. In the presence of the Coulomb interaction, two-electron states may be employed as a basis set for constructing the anticrossing-level states [1] when two electrons travel ballistically along a quasi-1D channel. The corresponding calculations have shown that the significance of the Coulomb induced level anticrossing within a quantum wire may be adjusted by varying the confinement potential with a top gate voltage [15].

There has been related work on conductance measurements of a quasi-1D wire having a quantum dot within the channel due to the presence of an impurity, as well as imperfections in the device geometry [16]. These undesired features may
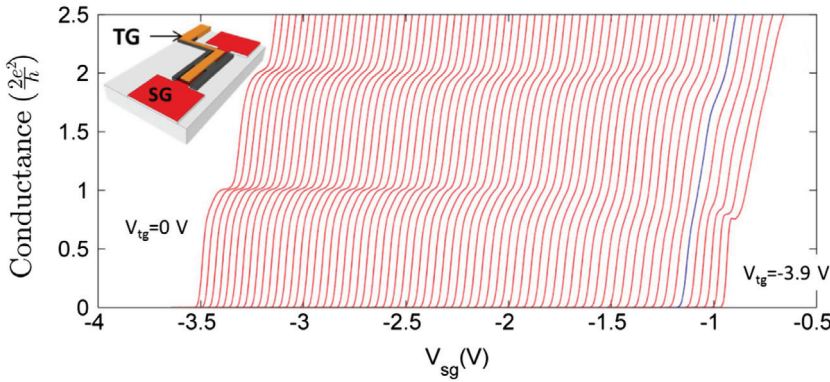
Figure 1. (Color online) Schematic illustration of a device used in our experiments (left-upper corner), including a pair of split gates and a top gate.

Notes: Additionally, typical measured conductance features of the device are also shown as a function of split-gate voltage, V_{sg} for various fixed top-gate voltages, V_{tg}.

result in results differing from integer multiples of $2\,e^2/h$ for the conductance steps [17] or oscillations superimposed on the conductance trace [18]. Electron tunneling through the quantum dot in the channel as well as interference effects due to electron back-scattering from an impurity potential are believed to be responsible for these deviations in the values of the conductance plateaus of narrow quantum wires [18].

In the next section, we present a theoretical approach for calculating the conductance for a quasi-1D quantum wire at a low density of electrons. For this, we calculate the lowest energy eigenstates for a pair of interacting electrons within a confinement region. We explicitly determine the ground state of a dilute electron liquid and consequently the lowest conductance plateau. The complex two-electron tunneling [19,20] is not included in this review since it does not contribute to the formation of conductance-plateaus. Furthermore, we highlight below that there is a range of wire widths for which two-electron transport is mediated by anticrossing-level states based on the Coulomb interaction, and, therefore, it is not possible to describe the conductance by using a single-particle formalism.

2. Theoretical formulation of the problem

We will exploit the results for the eigenstates of a pair of interacting electrons within a harmonic confining potential [21,22]. In Ref. [21], a symmetric harmonic potential was introduced. According to Kohn's theorem [22], for this potential the Coulomb interaction should only affect the relative motion of electrons but not that for the center-of-mass. It has been pointed out that as a perpendicular magnetic field is increased, the ground state will oscillate between a spin singlet and a spin triplet. Bryant [22] showed these electron correlation effects depend on the area of containment. By solving the Schrödinger equation

exactly for two interacting electrons, it becomes clear how correlations may select the ground state and give rise to quasiparticles which participate in the transport.

Coherent wavefunctions of two interacting electrons may be maintained during their transport along the channel if scattering by randomly distributed impurities and defects (negligible lattice scattering at low temperatures) is very small for high-mobility short channel samples. Also, if the transmission coefficient for two injected electrons is almost perfect and the inelastic scattering between different two-electron states is nearly vanishing, we are able to use a quantum ballistic transport model for two interacting electrons then the Coulomb interaction between electrons in the channel can be fully taken into account. Ballistic transport of two-electron clusters is assumed along the channel (y) direction. However, the finite width of a conduction channel in the transverse x direction gives rise to quantization of the split cluster energy levels. Each level is assigned to have a free-electron-like kinetic energy for a ballistically moving noninteracting two-electron cluster. This leads to a hierarchy of subbands with quadratic wave-vector dependence. The cluster energy levels are given by $E_{j,k_y}^{(p)} = E_j^{(p)} + \hbar^2 k_y^2/m^*$ with label p and $j = 1, 2, 3, 4$, where k_y is the wave vector of electrons along the channel, m^* is the electron effective mass and the 'subband edges' $E_j^{(p)}$ are presented after Equation (27) in terms of the dimensionless Coulomb integrals. For a fixed linear electron density n_{1D}, the two-electron chemical potential $\mu_p(T, n_{1D})$ within the channel may be calculated using

$$n_{1D} = \frac{2}{\pi} \sum_{j=1}^{4} \int_0^{\infty} dk_y \left[\exp\left(\frac{E_{j,k_y}^{(p)} - \mu_p}{k_B T} \right) + 1 \right]^{-1} \tag{1}$$

which is expressed in terms of the temperature T of the system. Also, the chemical potentials for the left (L) and right (R) electrodes (with areal electron density n_{2D}) are $\mu_L^{(p)}(V_b, T, n_{2D}) = \mu_p(T, n_{1D}) + eV_b$ and $\mu_R^{(p)}(V_b, T, n_{2D}) = \mu_p(T, n_{1D}) - eV_b$, respectively, in the presence of a low biased voltage V_b.

For quantum ballistic charge/heat transport of two interacting electrons in the channel, the charge ($\alpha = 0$) and heat ($\alpha = 1$) current densities are calculated from [23]

$$J^{(\alpha)}(V_b, T, n_{1D}) = \frac{(-2e)^{1-\alpha}}{\pi} \sum_{j=1}^{4} \int_0^{\infty} dk_y \, (E_{j,k_y}^{(p)} - \mu_p)^{\alpha} \left| v_{j,k_y} \right| \\ \left[f_L(E_{j,k_y}^{(p)}) - f_R(E_{j,k_y}^{(p)}) \right], \tag{2}$$

where $v_{j,k_y} = \hbar k_y/m^*$ is the half of the total group velocity of the two-electron state, $f_L(E_{j,k_y}^{(p)})$ and $f_R(E_{j,k_y}^{(p)})$ are the Fermi functions for noninteracting two-electron states in the left (L) and right (R) electrodes with chemical potentials $\mu_L^{(p)}$ and $\mu_R^{(p)}$, respectively, for noninteracting two-electron states.

In formulating our theory, we start by considering two interacting electrons in an elongated quantum dot within a quantum wire. For this quantum dot, an anisotropic confinement is assumed with a shorter confining length ξ_x across the channel (x direction) with a longer confining length ξ_y along the channel (y direction). Here, the Hamiltonian for two interacting electrons can be written as

$$\hat{\mathcal{H}}(\mathbf{r}_1, \mathbf{r}_2) = \hat{\mathcal{H}}_0(\mathbf{r}_1) + \hat{\mathcal{H}}_0(\mathbf{r}_2) + \mathcal{U}_C(|\mathbf{r}_1 - \mathbf{r}_2|)$$

$$\hat{\mathcal{H}}_0(\mathbf{r}_i) = \frac{\hat{\mathbf{p}}_i^2}{2m^*} + \mathcal{V}_c(\mathbf{r}_i), \quad \mathcal{U}_C(|\mathbf{r}_1 - \mathbf{r}_2|) = \frac{e^2}{4\pi \epsilon_0 \epsilon_r |\mathbf{r}_1 - \mathbf{r}_2|}, \quad (3)$$

where $i = 1, 2$ labels each electron, $\hat{\mathbf{p}}_i = -i\hbar\nabla_{\mathbf{r}_i}$, $\mathcal{V}_c(\mathbf{r}_i)$ is the confining potential for the conduction channel, $\hat{\mathcal{H}}_0(\mathbf{r}_i)$ is the single-electron Hamiltonian, and $\mathcal{U}_C(|\mathbf{r}_1 - \mathbf{r}_2|)$ represents the electron–electron interaction in a medium with background dielectric constant ϵ_r.

The single-particle eigenstates $\phi_\alpha(\mathbf{r}) \equiv \langle \mathbf{r}|\phi_\alpha\rangle$ can be determined from the Schrödinger equation $\hat{\mathcal{H}}_0(\mathbf{r})\, \phi_\alpha(\mathbf{r}) = \varepsilon_\alpha\, \phi_\alpha(\mathbf{r})$, where the eigenfunctions $\{\phi_\alpha(\mathbf{r})\}$ constitute a complete orthonormal set $|\phi_\alpha\rangle$ in the single particle Hilbert space. After properly antisymmetrizing the two particle basis, including both the orbital and spin parts, we obtain

$$\Psi_{\alpha_m,\beta_n}(\mathbf{r}_1, s_1; \mathbf{r}_2, s_2) = \tfrac{1}{\sqrt{2}} \left[\phi_{\alpha_m}(\mathbf{r}_1)\chi_m(s_1)\, \phi_{\beta_n}(\mathbf{r}_2)\chi_n(s_2) \right.$$
$$\left. - \phi_{\beta_n}(\mathbf{r}_1)\chi_n(s_1)\, \phi_{\alpha_m}(\mathbf{r}_2)\chi_m(s_2) \right], \quad (4)$$

where $\chi_m(s_i)$ is the spinor for the spin state of an electron. Here, the basis states in Equation (4) are degenerate eigenstates of the noninteracting Hamiltonian $\hat{\mathcal{H}}_0(\mathbf{r}_1, \mathbf{r}_2) \equiv \hat{\mathcal{H}}_0(\mathbf{r}_1) + \hat{\mathcal{H}}_0(\mathbf{r}_2)$ with $\hat{\mathcal{H}}_0(\mathbf{r}_1, \mathbf{r}_2)\, \Psi_{\alpha_m,\beta_n}(\mathbf{r}_1, s_1; \mathbf{r}_2, s_2) = (\varepsilon_{\alpha_m} + \varepsilon_{\beta_n})\, \Psi_{\alpha_m,\beta_n}(\mathbf{r}_1, s_1; \mathbf{r}_2, s_2)$. We restrict ourselves in the following to the case when only the lowest two orbitals $\alpha_m = \alpha$ and $\beta_n = \beta$ are populated.

If we assume that two electrons stay in the same spin state with $\chi_1 = \chi_2 = |\uparrow\rangle$, the spinor part can be factored out, giving rise to

$$\Psi(\mathbf{r}_1, s_1; \mathbf{r}_2, s_2) = \frac{1}{\sqrt{2}} \left[\phi_\alpha(\mathbf{r}_1)\, \phi_\beta(\mathbf{r}_2) - \phi_\beta(\mathbf{r}_1)\, \phi_\alpha(\mathbf{r}_2) \right] \chi_1(s_1)\chi_1(s_2). \quad (5)$$

However, if we assume that two electrons remain in opposite spin state with $\chi_1 = |\uparrow\rangle$ and $\chi_2 = |\downarrow\rangle$, then the result becomes

$$\Psi(\mathbf{r}_1, s_1; \mathbf{r}_2, s_2) = \frac{1}{\sqrt{2}} \left[\phi_\alpha(\mathbf{r}_1)\chi_1(s_1)\, \phi_\beta(\mathbf{r}_2)\chi_2(s_2) - \phi_\beta(\mathbf{r}_1)\chi_2(s_1)\, \phi_\alpha(\mathbf{r}_2)\chi_1(s_2) \right].$$
$$(6)$$

Consequently, the subspace of the lowest states for two independent electrons can be spanned by the following basis [24]

$$|\Psi_1(\mathbf{r}_1, s_1; \mathbf{r}_2, s_2)\rangle = \frac{1}{\sqrt{2}} \phi_\alpha(\mathbf{r}_1)\phi_\alpha(\mathbf{r}_2) \left(|\uparrow\rangle_1|\downarrow\rangle_2 - |\downarrow\rangle_1|\uparrow\rangle_2\right),$$

$$|\Psi_2(\mathbf{r}_1, s_1; \mathbf{r}_2, s_2)\rangle = \frac{1}{\sqrt{2}} \phi_\beta(\mathbf{r}_1)\phi_\beta(\mathbf{r}_2) \left(|\uparrow\rangle_1|\downarrow\rangle_2 - |\downarrow\rangle_1|\uparrow\rangle_2\right),$$

$$|\Psi_3(\mathbf{r}_1, s_1; \mathbf{r}_2, s_2)\rangle = \frac{1}{2} \left[\phi_\alpha(\mathbf{r}_1)\phi_\beta(\mathbf{r}_2) + \phi_\beta(\mathbf{r}_1)\phi_\alpha(\mathbf{r}_2)\right] \left(|\uparrow\rangle_1|\downarrow\rangle_2 - |\downarrow\rangle_1|\uparrow\rangle_2\right),$$

$$|\Psi_4(\mathbf{r}_1, s_1; \mathbf{r}_2, s_2)\rangle = \frac{1}{\sqrt{2}} \left[\phi_\alpha(\mathbf{r}_1)\phi_\beta(\mathbf{r}_2) - \phi_\beta(\mathbf{r}_1)\phi_\alpha(\mathbf{r}_2)\right] |\uparrow\rangle_1|\uparrow\rangle_2,$$

$$|\Psi_5(\mathbf{r}_1, s_1; \mathbf{r}_2, s_2)\rangle = \frac{1}{\sqrt{2}} \left[\phi_\alpha(\mathbf{r}_1)\phi_\beta(\mathbf{r}_2) - \phi_\beta(\mathbf{r}_1)\phi_\alpha(\mathbf{r}_2)\right] |\downarrow\rangle_1|\downarrow\rangle_2,$$

$$|\Psi_6(\mathbf{r}_1, s_1; \mathbf{r}_2, s_2)\rangle = \frac{1}{2} \left[\phi_\alpha(\mathbf{r}_1)\phi_\beta(\mathbf{r}_2) - \phi_\beta(\mathbf{r}_1)\phi_\alpha(\mathbf{r}_2)\right] \left(|\uparrow\rangle_1|\downarrow\rangle_2 + |\downarrow\rangle_1|\uparrow\rangle_2\right)$$

$$(7)$$

Here, the six components of these two-electron sets are orthonormal, i.e. $\langle\Psi_m|\Psi_n\rangle = \delta_{m,n}$. Moreover, using the above six states, the interacting Hamiltonian matrix can be cast into the form of

$$\hat{\mathcal{H}} = \begin{pmatrix} 2\varepsilon_\alpha + U_{11} & U_{12} & U_{13} & 0 & 0 & 0 \\ U_{21} & 2\varepsilon_\beta + U_{22} & U_{23} & 0 & 0 & 0 \\ U_{31} & U_{32} & \varepsilon_\alpha + \varepsilon_\beta + U_{33} & 0 & 0 & 0 \\ 0 & 0 & 0 & \varepsilon_\alpha + \varepsilon_\beta + U_{44} & 0 & 0 \\ 0 & 0 & 0 & 0 & \varepsilon_\alpha + \varepsilon_\beta + U_{55} & 0 \\ 0 & 0 & 0 & 0 & 0 & \varepsilon_\alpha + \varepsilon_\beta + U_{66} \end{pmatrix}$$

$$(8)$$

where $U_{mn} = \langle\Psi_m|\mathcal{U}_C|\Psi_n\rangle = U_{nm}^*$ is the Coulomb matrix element. Explicitly, we define the notations for the Coulomb matrix elements as

$$\mathcal{M}_{\alpha\beta;\,\alpha'\beta'} \equiv \langle\phi_\alpha, \phi_\beta|\mathcal{U}_C|\phi_{\alpha'}, \phi_{\beta'}\rangle,$$

$$\mathcal{M}_{\beta\alpha;\,\beta'\alpha'} = \mathcal{M}_{\alpha\beta;\,\alpha'\beta'}. \qquad (9)$$

Introducing the Fourier transform to the Coulomb potential, we are able to express its matrix elements using the Coulomb and exchange integrals, i.e.

$$\frac{1}{|\mathbf{r}_1 - \mathbf{r}_2|} = \int \frac{d^2\mathbf{q}}{2\pi} \frac{e^{i\mathbf{q}\cdot(\mathbf{r}_1-\mathbf{r}_2)}}{|\mathbf{q}|}. \qquad (10)$$

This gives rise to

$$U_{11} = \mathcal{M}_{\alpha\alpha;\,\alpha\alpha} \equiv \langle\phi_\alpha, \phi_\alpha|\mathcal{U}_C|\phi_\alpha, \phi_\alpha\rangle$$

$$= \frac{e^2}{2\epsilon_0\epsilon_r} \int d^2\mathbf{q} \frac{|\mathcal{F}_{\alpha\alpha}(\mathbf{q})|^2}{|\mathbf{q}|}, \qquad (11)$$

where we have employed the form factor, given by

$$\mathcal{F}_{\alpha\beta}(\mathbf{q}) = \frac{1}{2\pi} \int d^2\mathbf{r}\, \phi_\alpha^*(\mathbf{r})\, e^{i\mathbf{q}\cdot\mathbf{r}}\, \phi_\beta(\mathbf{r}) = \mathcal{F}_{\beta\alpha}^*(-\mathbf{q}). \tag{12}$$

Similarly, we can obtain other nonzero matrix elements from

$$U_{22} = \mathcal{M}_{\beta\beta;\,\beta\beta} = \frac{e^2}{2\epsilon_0\epsilon_r} \int \frac{d^2\mathbf{q}}{|\mathbf{q}|} \left|\mathcal{F}_{\beta\beta}(\mathbf{q})\right|^2 ,$$

$$U_{12} = \mathcal{M}_{\alpha\alpha;\,\beta\beta} = \frac{e^2}{2\epsilon_0\epsilon_r} \int \frac{d^2\mathbf{q}}{|\mathbf{q}|} \mathcal{F}_{\alpha\beta}(\mathbf{q})\mathcal{F}_{\alpha\beta}(-\mathbf{q}) ,$$

$$U_{13} = \frac{1}{\sqrt{2}} \left(\mathcal{M}_{\alpha\alpha;\,\alpha\beta} + \mathcal{M}_{\alpha\alpha;\,\beta\alpha} \right)$$

$$= \frac{e^2}{2\sqrt{2}\epsilon_0\epsilon_r} \int \frac{d^2\mathbf{q}}{|\mathbf{q}|} \left[\mathcal{F}_{\alpha\alpha}(\mathbf{q})\mathcal{F}_{\alpha\beta}(-\mathbf{q}) + \mathcal{F}_{\alpha\beta}(\mathbf{q})\mathcal{F}_{\alpha\alpha}(-\mathbf{q}) \right] ,$$

$$U_{23} = \frac{1}{\sqrt{2}} \left(\mathcal{M}_{\beta\beta;\,\alpha\beta} + \mathcal{M}_{\beta\beta;\,\beta\alpha} \right)$$

$$= \frac{e^2}{2\sqrt{2}\epsilon_0\epsilon_r} \int \frac{d^2\mathbf{q}}{|\mathbf{q}|} \left[\mathcal{F}_{\beta\alpha}(\mathbf{q})\mathcal{F}_{\beta\beta}(-\mathbf{q}) + \mathcal{F}_{\beta\beta}(\mathbf{q})\mathcal{F}_{\beta\alpha}(-\mathbf{q}) \right] ,$$

$$U_{33} = \mathcal{M}_{\alpha\beta;\,\alpha\beta} + \mathcal{M}_{\alpha\beta;\,\beta\alpha} = \frac{e^2}{2\epsilon_0\epsilon_r} \int \frac{d^2\mathbf{q}}{|\mathbf{q}|} \left[\mathcal{F}_{\alpha\alpha}(\mathbf{q})\mathcal{F}_{\beta\beta}(-\mathbf{q}) + \left|\mathcal{F}_{\alpha\beta}(\mathbf{q})\right|^2 \right] ,$$

$$U_{44} = \mathcal{M}_{\alpha\beta;\,\alpha\beta} - \mathcal{M}_{\alpha\beta;\,\beta\alpha} = \frac{e^2}{2\epsilon_0\epsilon_r} \int \frac{d^2\mathbf{q}}{|\mathbf{q}|} \left[\mathcal{F}_{\alpha\alpha}(\mathbf{q})\mathcal{F}_{\beta\beta}(-\mathbf{q}) - \left|\mathcal{F}_{\alpha\beta}(\mathbf{q})\right|^2 \right]$$

$$= U_{55} = U_{66} . \tag{13}$$

After we diagonalize the Hamiltonian matrix in Equation (8), both the energy eigenvalues and associated eigenstates can be obtained in a straightforward way.

Now, let us consider explicitly a harmonic confining potential for electrons within the $xy-$plane, i.e.

$$\mathcal{V}_c(\mathbf{r}) = \frac{1}{2} m^* \left(\omega_x^2 x^2 + \omega_y^2 y^2 \right) , \tag{14}$$

with $\omega_y \ll \omega_x$. As a result, the orbital parts of the single-particle eigenstates can be written down as

$$\phi_{m,n}(x, y) = \psi_m(x)\, \psi_n(y) , \quad \varepsilon_{m,n} = \hbar\omega_x \left(m + 1/2 \right) + \hbar\omega_y \left(n + 1/2 \right) . \tag{15}$$

We will choose two eigenstates, $\phi_\alpha(x, y) = \psi_0(x)\, \psi_0(y)$ and $\phi_\beta(x, y) = \psi_1(x) \psi_0(y)$, where $\psi_n(x)$ is the one-dimensional oscillator wavefunction for $n = 0, 1, 2, \cdots$. This yields

$$\phi_\alpha(x, y) = \left(\frac{1}{\pi \xi_x \xi_y}\right)^{1/2} \exp\left(-\frac{x^2}{2\xi_x^2}\right) \exp\left(-\frac{y^2}{2\xi_y^2}\right),$$

$$\mathcal{F}_{\alpha\alpha}(\mathbf{q}) = \frac{1}{2\pi} \exp\left(-\frac{q_x^2 \xi_x^2}{4}\right) \exp\left(-\frac{q_y^2 \xi_y^2}{4}\right), \tag{16}$$

as well as

$$\phi_\beta(x, y) = \left(\frac{1}{2\pi \xi_x \xi_y}\right)^{1/2} \left(\frac{2x}{\xi_x}\right) \exp\left(-\frac{x^2}{2\xi_x^2}\right) \exp\left(-\frac{y^2}{2\xi_y^2}\right),$$

$$\mathcal{F}_{\beta\beta}(\mathbf{q}) = \frac{1}{4\pi} \left(2 - q_x^2 \xi_x^2\right) \exp\left(-\frac{q_x^2 \xi_x^2}{4}\right) \exp\left(-\frac{q_y^2 \xi_y^2}{4}\right),$$

$$\mathcal{F}_{\alpha\beta}(\mathbf{q}) = \frac{iq_x \xi_x}{2\pi\sqrt{2}} \exp\left(-\frac{q_x^2 \xi_x^2}{4}\right) \exp\left(-\frac{q_y^2 \xi_y^2}{4}\right). \tag{17}$$

Here, $\xi_x = \sqrt{\hbar/m^*\omega_x}$ and $\xi_y = \sqrt{\hbar/m^*\omega_y}$ are the confining lengths, and then, the system dimension may be significantly larger along the y-direction compared to that in the x-direction.

We know from Equations (15) and (16) that eigenstates $\phi_\alpha(\mathbf{r})$ and $\phi_\beta(\mathbf{r})$ have opposite parity. Consequently, we find $\mathcal{F}_{\alpha\alpha}(\mathbf{q}) = \mathcal{F}_{\alpha\alpha}(-\mathbf{q})$, $\mathcal{F}_{\beta\beta}(\mathbf{q}) = \mathcal{F}_{\beta\beta}(-\mathbf{q})$, and $\mathcal{F}_{\alpha\beta}(\mathbf{q}) + \mathcal{F}_{\alpha\beta}(-\mathbf{q}) = 0$. This directly leads to $u_{13} = u_{23} = 0$. Moreover, for a harmonic potential the block part of the truncated Hamiltonian in Equation (8) becomes

$$\hat{\mathcal{H}}_{3\times3} = \begin{pmatrix} 2\varepsilon_\alpha + U_{11} & U_{12} & 0 \\ U_{12} & 2\varepsilon_\beta + U_{22} & 0 \\ 0 & 0 & \varepsilon_\alpha + \varepsilon_\beta + U_{33} \end{pmatrix}. \tag{18}$$

From this, we obtain two split energy eigenvalues for the states Ψ_1 and Ψ_2, given by

$$E_{1,2} \equiv E_\pm = \varepsilon_\alpha + \varepsilon_\beta + \frac{1}{2}\left(U_{11} + U_{22}\right) \pm \mathcal{D}, \tag{19}$$

and the uncoupled energy level $E_3 = \varepsilon_\alpha + \varepsilon_\beta + U_{33}$ for the state Ψ_3, as well as the triple-degenerate energy levels $E_4 = E_5 = E_6 = \varepsilon_\alpha + \varepsilon_\beta + U_{44}$ for the states Ψ_4, Ψ_5, and Ψ_6. In Equaion (19), the energy-level coupling $\mathcal{D} = \sqrt{[\varepsilon_\beta - \varepsilon_\alpha + (U_{22} - U_{11})/2]^2 + |U_{12}|^2}$, and the level splitting is $E_+ - E_- = 2\mathcal{D} > 0$.

For evaluating u_{11}, u_{22}, u_{33}, u_{12}, and u_{44}, we require the following Coulomb integrals:

$$\mathcal{I}_{\alpha\alpha;\alpha\alpha} = 2\pi L_y \int \frac{d^2\mathbf{q}}{|\mathbf{q}|} \left|\mathcal{F}_{\alpha\alpha}(\mathbf{q})\right|^2 = \frac{L_y}{2\pi} \int_0^{2\pi} d\theta \int_0^\infty dq\, e^{-\alpha(\theta)q^2}$$

$$= \frac{L_y}{4\sqrt{\pi}} \int_0^{2\pi} \frac{d\theta}{\sqrt{\alpha(\theta)}}$$

$$= \frac{L_y}{\sqrt{2\pi}} \int_0^\pi \frac{d\theta}{(\xi_x^2 \cos^2\theta + \xi_y^2 \sin^2\theta)^{1/2}}$$

$$= \frac{L_y}{\sqrt{2\pi}\xi_y} \int_0^\pi \frac{d\theta}{[1 + (\gamma^2 - 1)\cos^2\theta]^{1/2}}, \tag{20}$$

where we have used $q_x = q\cos\theta$, $q_y = q\sin\theta$, θ is the angle between the wave vector $\mathbf{q}$ and x axis, $\gamma \equiv \xi_x/\xi_y$, and $\alpha(\theta) = (\xi_x^2 \cos^2\theta + \xi_y^2 \sin^2\theta)/2$. Additionally, we obtain

$$\mathcal{I}_{\beta\beta;\,\beta\beta} = 2\pi L_y \int \frac{d^2\mathbf{q}}{|\mathbf{q}|} |\mathcal{F}_{\beta\beta}(\mathbf{q})|^2$$

$$= \frac{L_y}{8\pi} \int_0^{2\pi} d\theta \int_0^\infty dq \, (2 - q^2 \xi_x^2 \cos^2\theta)^2 \, e^{-\alpha(\theta)q^2}$$

$$= \frac{L_y}{4\pi} \int_0^\pi d\theta \left[I_1(\theta) + I_2(\theta) + I_3(\theta) \right], \tag{21}$$

where

$$I_1(\theta) = 4 \int_0^\infty dq \, e^{-\alpha(\theta)q^2} = \frac{2\sqrt{\pi}}{\sqrt{\alpha(\theta)}},$$

$$I_2(\theta) = -4\xi_x^2 \cos^2\theta \int_0^\infty dq \, q^2 \, e^{-\alpha(\theta)q^2} = -\frac{\sqrt{\pi}\xi_x^2 \cos^2\theta}{\sqrt{\alpha^3(\theta)}},$$

$$I_3(\theta) = \xi_x^4 \cos^4\theta \int_0^\infty dq \, q^4 \, e^{-\alpha(\theta)q^2} = \frac{3\sqrt{\pi}\xi_x^4 \cos^4\theta}{8\sqrt{\alpha^5(\theta)}}. \tag{22}$$

By combining the results for $I_1(\theta)$, $I_2(\theta)$, and $I_3(\theta)$, this leads to

$$\mathcal{I}_{\beta\beta;\,\beta\beta} = \frac{L_y}{\sqrt{2\pi}} \int_0^\pi \frac{d\theta}{(\xi_x^2 \cos^2\theta + \xi_y^2 \sin^2\theta)^{1/2}}$$

$$\times \left[1 - \frac{\xi_x^2 \cos^2\theta}{\xi_x^2 \cos^2\theta + \xi_y^2 \sin^2\theta} + \frac{3\xi_x^4 \cos^4\theta}{4(\xi_x^2 \cos^2\theta + \xi_y^2 \sin^2\theta)^2} \right]$$

$$= \frac{L_y}{\sqrt{2\pi}\xi_y} \int_0^\pi \frac{d\theta}{[1 + (\gamma^2 - 1)\cos^2\theta]^{1/2}}$$

$$\times \left[1 - \frac{\gamma^2 \cos^2\theta}{1 + (\gamma^2 - 1)\cos^2\theta} + \frac{3\gamma^4 \cos^4\theta}{4[1 + (\gamma^2 - 1)\cos^2\theta]^2} \right]. \tag{23}$$

In a similar way, we find

$$
\begin{aligned}
\mathcal{I}_{\alpha\beta;\,\alpha\beta} &= 2\pi L_y \int \frac{\mathrm{d}^2\mathbf{q}}{|\mathbf{q}|}\, \mathcal{F}_{\alpha\alpha}(\mathbf{q})\mathcal{F}_{\beta\beta}(-\mathbf{q}) \\
&= \frac{L_y}{4\pi} \int_0^{2\pi} \mathrm{d}\theta \int_0^{\infty} \mathrm{d}q \left(2 - q^2\xi_x^2 \cos^2\theta\right) e^{-\alpha(\theta)q^2} \\
&= \frac{L_y}{2\pi} \int_0^{\pi} \mathrm{d}\theta \left[J_1(\theta) + J_2(\theta)\right],
\end{aligned}
\tag{24}
$$

where

$$
\begin{aligned}
J_1(\theta) &= 2 \int_0^{\infty} \mathrm{d}q\, e^{-\alpha(\theta)q^2} = \frac{\sqrt{\pi}}{\sqrt{\alpha(\theta)}}, \\
J_2(\theta) &= -\xi_x^2 \cos^2\theta \int_0^{\infty} \mathrm{d}q\, q^2\, e^{-\alpha(\theta)q^2} = -\frac{\sqrt{\pi}\xi_x^2 \cos^2\theta}{4\sqrt{\alpha^3(\theta)}}.
\end{aligned}
\tag{25}
$$

By combining these results for $J_1(\theta)$ and $J_2(\theta)$, we have

$$
\begin{aligned}
\mathcal{I}_{\alpha\beta;\,\alpha\beta} &= \frac{L_y}{\sqrt{2\pi}} \int_0^{\pi} \frac{\mathrm{d}\theta}{(\xi_x^2 \cos^2\theta + \xi_y^2 \sin^2\theta)^{1/2}} \left[1 - \frac{\xi_x^2 \cos^2\theta}{2(\xi_x^2 \cos^2\theta + \xi_y^2 \sin^2\theta)}\right] \\
&= \frac{L_y}{\sqrt{2\pi}\xi_y} \int_0^{\pi} \frac{\mathrm{d}\theta}{[1 + (\gamma^2 - 1)\cos^2\theta]^{1/2}} \left[1 - \frac{\gamma^2 \cos^2\theta}{2[1 + (\gamma^2 - 1)\cos^2\theta]}\right] \\
&= \frac{L_y}{2\sqrt{2\pi}\xi_y} \int_0^{\pi} \mathrm{d}\theta\, \frac{2 + (\gamma^2 - 1)\cos^2\theta}{[1 + (\gamma^2 - 1)\cos^2\theta]^{3/2}}.
\end{aligned}
\tag{26}
$$

The last integral is calculated as

$$
\begin{aligned}
\mathcal{I}_{\alpha\beta;\,\beta\alpha} = I_{\alpha\alpha;\,\beta\beta} &= 2\pi L_y \int \frac{\mathrm{d}^2\mathbf{q}}{|\mathbf{q}|}\,|\,\mathcal{F}_{\alpha\beta}(\mathbf{q})\mathcal{F}_{\alpha\beta}(-\mathbf{q}) \\
&= \frac{L_y}{4\pi} \int_0^{2\pi} \mathrm{d}\theta \int_0^{\infty} \mathrm{d}q\, q^2\xi_x^2 \cos^2\theta\, e^{-\alpha(\theta)q^2} \\
&= \frac{L_y}{8\sqrt{\pi}} \int_0^{\pi} \mathrm{d}\theta\, \frac{\xi_x^2 \cos^2\theta}{\sqrt{\alpha^3(\theta)}} = \frac{1}{2\sqrt{2\pi}} \int_0^{\pi} \mathrm{d}\theta\, \frac{\xi_x^2 \cos^2\theta}{(\xi_x^2 \cos^2\theta + \xi_y^2 \sin^2\theta)^{3/2}} \\
&= \frac{L_y}{2\sqrt{2\pi}\xi_y} \int_0^{\pi} \mathrm{d}\theta\, \frac{\gamma^2 \cos^2\theta}{[1 + (\gamma^2 - 1)\cos^2\theta]^{3/2}}.
\end{aligned}
\tag{27}
$$

It is important to note that we have assumed a quasi-continuum energy spectrum for a traveling quasiparticle in the longitudinal direction, in contrast with split energy levels in the transverse direction. In this case, the pair of electrons forming the quasiparticle always have the lowest transverse energy plus a free electron-like kinetic energy, resulting from the longitudinal motion. However, the Coulomb interaction between a pair of electrons in this cluster

will significantly modify the 'subband edges' $(E_j^{(p)})$ due to quantization in the transverse direction.

All quasiparticles, except the transported one, may be treated as a 'background' making up the total electron density and have a quasiparticle chemical potential μ_p which is determined using Equation (1). For the interacting two-electron states, by using the above derivations, their energy levels $E_j^{(p)} = E_{j,k_y=0}^{(p)}$ are calculated as $E_1^{(p)} \equiv E_-^{(p)} = \varepsilon_0 + \varepsilon_1 + (u_{11} + u_{22})/2 - \Delta_C$, $E_2^{(p)} \equiv E_+^{(p)} = \varepsilon_0 + \varepsilon_1 + (u_{11} + u_{22})/2 + \Delta_C$, $E_3^{(p)} = \varepsilon_0 + \varepsilon_1 + u_{33}$, and $E_4^{(p)} = \varepsilon_0 + \varepsilon_1 + u_{44}$, where that Coulomb coupling term for the two-electron anticrossing states is given by $\Delta_C = \sqrt{[\varepsilon_1 - \varepsilon_0 + (u_{22} - u_{11})/2]^2 + |u_{12}|^2}$. In this notation, the single-particle energy levels for the harmonic-potential model with anisotropic harmonic frequencies ω_x and ω_y in the transverse (x) and longitudinal (y) directions, respectively, are: $\varepsilon_0 = (\hbar\omega_x + \hbar\omega_y)/2$ and $\varepsilon_1 = (3\hbar\omega_x + \hbar\omega_y)/2$, while the introduced Coulomb interaction energies are found to be $u_{11}/E_c = N_0^2 \mathcal{I}_{00,00}$, $u_{12}/E_c = N_0 N_1 \mathcal{I}_{00,11}$, $u_{22}/E_c = N_1^2 \mathcal{I}_{11,11}$, $u_{33}/E_c = N_0 N_1 (\mathcal{I}_{01,01} + \mathcal{I}_{01,10})$, and $u_{44}/E_c = N_0 N_1 (3\mathcal{I}_{01,01} - \mathcal{I}_{01,10})$, where $E_c = e^2/4\pi\epsilon_0\epsilon_r L_y$ in terms of the channel length L_y and the background dielectric constant ϵ_r, $N_n = \{\exp[(\varepsilon_n - \mu_0)/k_B T] + 1\}^{-1}$ ($n = 0, 1$) is the single-particle level occupation factor, and $\mu_0(T, n_{1D})$ is the single-electron chemical potential within the channel. At the time when a quasiparticle enters a conduction channel, it will occupy single-particle energy levels ε_0 and ε_1, i.e. occupying the same one or different levels. Such a selection is determined from the subband occupation by the sea of electrons within the channel. After these two noninteracting electrons are injected into the channel, they will interact with each other through either the intrasubband or intersubband Coulomb coupling. The ballistic injection of two noninteracting electrons and the existence of a sea of electrons in the conduction channel are reflected through the inclusion of these two level occupation factors. The Coulomb integral is represented by $\mathcal{I}_{\alpha\beta,\alpha'\beta'}(\gamma)$ for $\alpha, \beta, \alpha', \beta' = 0, 1$ if we only consider interacting electron states formed from the lowest ('0') and first excited ('1') single-particle states.

The channel width W_x and length L_y are directly related to the frequencies ω_x and ω_y of the 2D harmonic-confining potential by $W_x = \sqrt{4\hbar/m^*\omega_x}$ and $L_y = \sqrt{4\hbar/m^*\omega_y}$, respectively. Therefore, we get the simple relations, i.e. $\xi_x = \sqrt{\hbar/m^*\omega_x} = W_x/2$, $\xi_y = \sqrt{\hbar/m^*\omega_y} = L_y/2$, and $\gamma \equiv \xi_x/\xi_y = W_x/L_y \equiv \mathcal{R}$. Furthermore, for $\mathcal{R} \gg 1$, we find that $\mathcal{I}_{\alpha\beta,\alpha',\beta'}(\mathcal{R})$ scales as $1/\mathcal{R}$ for $\alpha, \beta, \alpha', \beta' = 0, 1$.

In the random-phase approximation, the static dielectric function at low temperature for screening for an electron density n_{1D} and ϵ_r in the channel, may be expressed as [25]

$$\epsilon_{1D}(q) = 1 - \left(\frac{m^* e^2}{2\pi \epsilon_0 \epsilon_r \hbar^2 n_{1D}} \right) \ln \left(\frac{|q| W_x}{2} \right) , \qquad (28)$$

where the wave vector $q \sim k_F = \pi n_{1D}/2$. For the parameters chosen in our numerical calculations, we found that the effect due to static screening may be neglected. On the other hand, the static dielectric function for shielding by surface gate electrodes of the electron–electron interaction may be modeled as $\epsilon_G(q) = 1 + \coth(qd)$, for which we may take $q \sim k_F = \pi n_{1D}/2$ and d represents the gate insulator thickness [26]. For the parameters used in our numerical calculations, we found that shielding of the interaction between two-electron states may also be neglected.

From the calculated $J^{(\alpha=0)}(V_b, T, n_{1D})$ in Equation (2), the electrical conductance $G(T, n_{1D})$ for interacting two-electrons may be expressed as [23]

$$G(T, n_{1D}) = \frac{J^{(\alpha=0)}(V_b, T, n_{1D})}{V_b} . \qquad (29)$$

We now present our numerical results and their relationship to recently report experimental data in Ref. [1].

3. Numerical results and experimental data

In our numerical calculations, we use the following parameters: $T = 10\,\text{mK}$, $V_b = 0.01\,\text{mV}$, $L_y = 400\,\text{nm}$, $\epsilon_r = 12$, $m^* = 0.067\,m_0$ (m_0 is the free-electron mass). The chosen $\mathcal{R}$ values are indicated in the figure captions. Specifically, we denote the quantum ballistic transport of two-electron states with anticrossing levels through a conduction channel as one moving through either one of two states $E_{\pm}^{(p)}$.

For clarity, we point out that as two electrons are injected into a conduction channel, they may occupy specific single-particle subbands for their ballistic transport. The selection rule is determined by the occupation factor of the electrons already sustained within the conduction channel. During the time interval that the two injected moving electrons remain within the channel, they may interact with each other through either the intrasubband or the intersubband Coulomb coupling. We emphasize that the linear density for confined electrons within the channel may be kept constant even when the channel width is varied. However, for this to occur, the Fermi energy must automatically adjust itself to accommodate all electrons and additional subbands will be populated with reduced energy level separations. Specifically, although the Fermi energy is reduced, the number of electrons in the channel is not changed at all. Furthermore, even when the Fermi energy is reduced, the second level can still be populated due to reduced level separation at the same time so as to keep the number of electrons in the channel a constant. Clearly, enhancement of the Coulomb interaction is not solely determined by the electron density, since it also

depends on how electrons are distributed. For the Coulomb effect on the two-electron states, the inclusion of a new populated two-electron state, where one electron stays in a lower-energy level while the other electron populates a higher level, will introduce a new Coulomb-interaction channel for the two-electron states.

3.1. Two-electron energies within the channel

We know that as the transverse confinement becomes weaker (or the $\mathcal{R}$ value is increased), the kinetic part of the energy levels $E_j^{(p)}$ of a two-electron state will decrease like as $1/\mathcal{R}^2$ for fixed L_y. On the other hand, the Coulomb interaction only scales as $1/\mathcal{R}$ as per our discussion preceding Equation (28). Consequently, the significance of the Coulomb interaction is expected to increase relatively by increasing $\mathcal{R}$. Moreover, the level separation will be reduced by increasing $\mathcal{R}$, leading to occupation of the second energy level for fixed electron density. Therefore, the additional Coulomb repulsion between two electrons on different single-particle energy levels must be considered. This effect can be seen from Figure 2(b)–(d) as the upward shifting of energy levels $E_-^{(p)}$ and $E_3^{(p)}$ (as $N_1 > 0$) in the region of $\mathcal{R} > 1$ as $n_{1D} \geq 0.2 \times 10^5$ cm^{-1}. At the same time, the $E_4^{(p)}$ level is pushed upward above the $E_3^{(p)}$ level due to the enhanced Coulomb interaction for $\mathcal{R} > 1$. On the other hand, for the $E_+^{(p)}$ two-electron state, which is associated with two excited-state electrons, it is largely dominated by the kinetic energy part for the whole range of $\mathcal{R}$ shown in this figure. When n_{1D} is further increased, the Coulomb repulsion effect pushes into the intermediate confinement regime ($\mathcal{R} \sim 1$) in Figure 2(d). Due to the combined effect of these two factors, we observe the recovery of the ground state $E_-^{(p)}$ level in Figure 2(d) for large values of $\mathcal{R}$ and n_{1D} (where the Coulomb energy is dominant) from that in Figure 2(a) for small values of $\mathcal{R}$ and n_{1D} (where the kinetic energy of electrons is dominant). It is interesting to see that the Coulomb interaction between electrons stands out to give rise to a pushing up of three energy levels and the recovery of the the ground $E_-^{(p)}$ level at the same time in an intermediate confinement regime ($\mathcal{R} \gtrsim 1$) between the strong (scaling as fast drop $1/\mathcal{R}^2$ for $\mathcal{R} < 1$) and weak (scaling as slow drop $1/\mathcal{R}$ for $\mathcal{R} \gg 1$) confinement regimes.

3.2. Ballistic conductance within a quasi-1D channel

The recovery of the ground-state in Figure 2 plays a significant role on both the distribution of conductance plateaus and the interplay from interaction effects, as displayed in Figure 3. We know the Coulomb coupling may be neglected for small n_{1D}, where the $2\,e^2/h$ conductance plateau is found for the interacting two-electron state as shown in 3(a) with almost all values of $\mathcal{R}$. As n_{1D} increases to 0.2×10^5 cm^{-1} in 3(b), the $2\,e^2/h$ plateau shown in 3(a) disappears except for its reappearance very close to $\mathcal{R} = 2.0$. If the value of n_{1D} gets even larger, as seen from Figure 3(c) and (d), the new $4\,e^2/h$ conductance plateau occurs for an
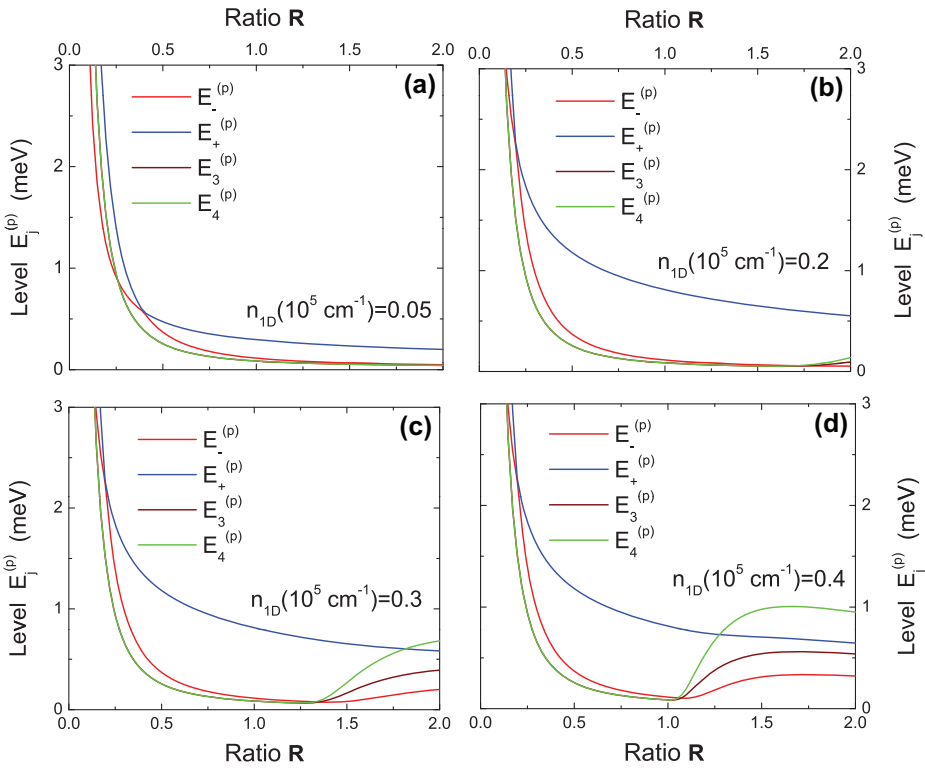
Figure 2. (Color online) Plots of cluster energy levels $E_j^{(p)}$ as a function of geometry ratio $\mathcal{R}$ with four different values of linear electron density n_{1D}.

interacting two-electron state, corresponding to the population of the degenerate lowest $E_3^{(p)}$ and $E_4^{(p)}$ energy levels after their level crossing with another $E_-^{(p)}$ state. However, when $\mathcal{R}$ further increases above one in the very-weak confinement regime, the ground-state recovery, as discussed in Figure 2(c) and (d), enforces the reoccurrence of the $2\,e^2/h$ conductance plateau due to the Coulomb repulsion between electrons in the central region of the channel.

3.3. Dependence of interacting electron energy on linear density

When electrons interact with each other, their energy levels $E_j^{(p)}$ are expected to depend on the electron density n_{1D}, as shown in Figure 4. When the geometry ratio $\mathcal{R} = W_x/L_y$ is small for strong confinement in Figure 4(a), only the ground state $E_-^{(p)}$ is affected by varying n_{1D} due primarily to $N_0 \neq 0$ in this case. As $\mathcal{R}$ is increased to 0.6 in Figure 4(b), both the level crossing between $E_-^{(p)}$ of the anticrossing state with the degenerate state $E_3^{(p)} = E_4^{(p)}$ and the level anticrossing between $E_-^{(p)}$ and $E_+^{(p)}$ states occur at lower densities. As $\mathcal{R} > 1$, the Coulomb interaction between electrons becomes much stronger, as presented in Figure 4(c) and (d). Therefore, both $E_3^{(p)}$ and $E_4^{(p)}$ levels are pushed up significantly at higher densities (i.e. $N_1 > 0$), leading to a recovery of the ground state to $E_-^{(p)}$. At
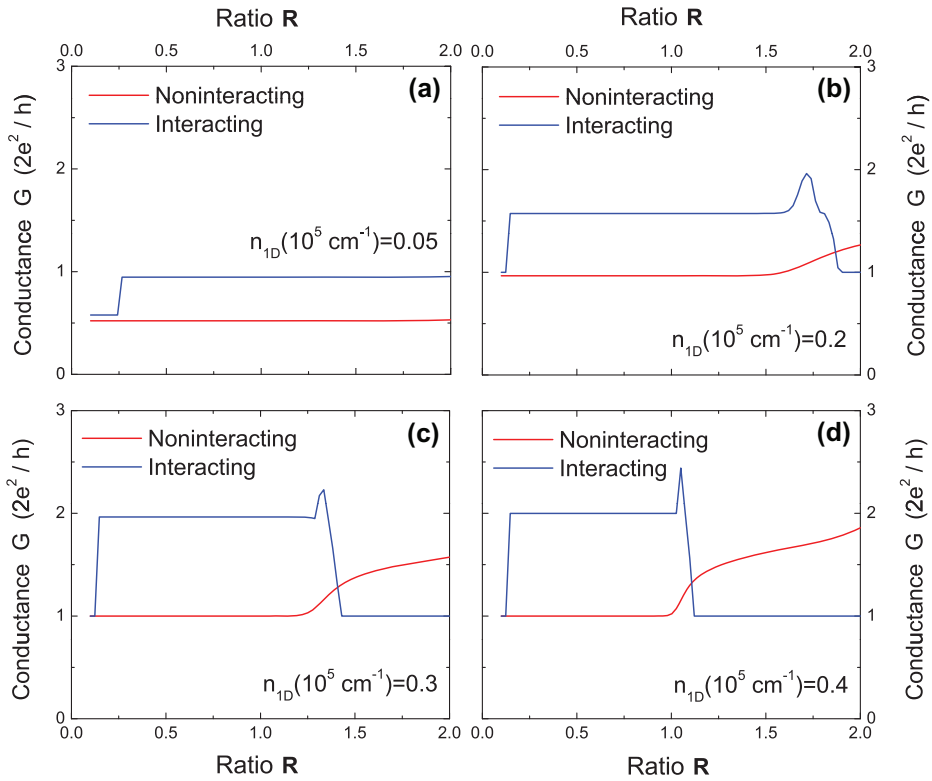
Figure 3. (Color online) Plots of conductance G as a function of geometry ratio $\mathcal{R}$ with four different values of linear electron density n_{1D} for both noninteracting and interacting cases.

the same time, the $E_4^{(p)}$ state in Figure 4(c) and (d) changes from the degenerate ground state at lower n_{1D} to the highest-energy state at higher n_{1D}. Furthermore, under a transverse magnetic field, we expect that the $E_3^{(p)}$ state should decouple from the magnetic field due to total spin $S = 0$, while the degenerate $E_4^{(p)}$ state with total spin $S = 1$ will be split into three by the Zeeman effect, leading to new e^2/h and $3\,e^2/h$ conductance plateaus [27].

3.4. Conductance for two interacting and noninteracting electron pairs

Figure 5 presents a comparison of the conductance G for both a noninteracting and interacting two-electron state in the range of $0.1 \leq \mathcal{R} \leq 1$. For very strong confinement in 4(a), the Coulomb-interaction effect becomes negligible in comparison with the dominant kinetic energy of electrons and a conductance $2\,e^2/h$ plateau remains with increasing n_{1D}. On the other hand, as $\mathcal{R}$ goes up to 0.4 in 5(b) and 0.6 in 5(c) for cases with strong confinement, although G for a noninteracting two-electron state remains largely unchanged, for an interacting two-electron state, the conductance $2\,e^2/h$ plateau in Figure 5(a) is completely destroyed by the Coulomb interaction and replaced by a new $4\,e^2/h$ plateau. This unique feature is attributed to the result of both a level-crossing and a
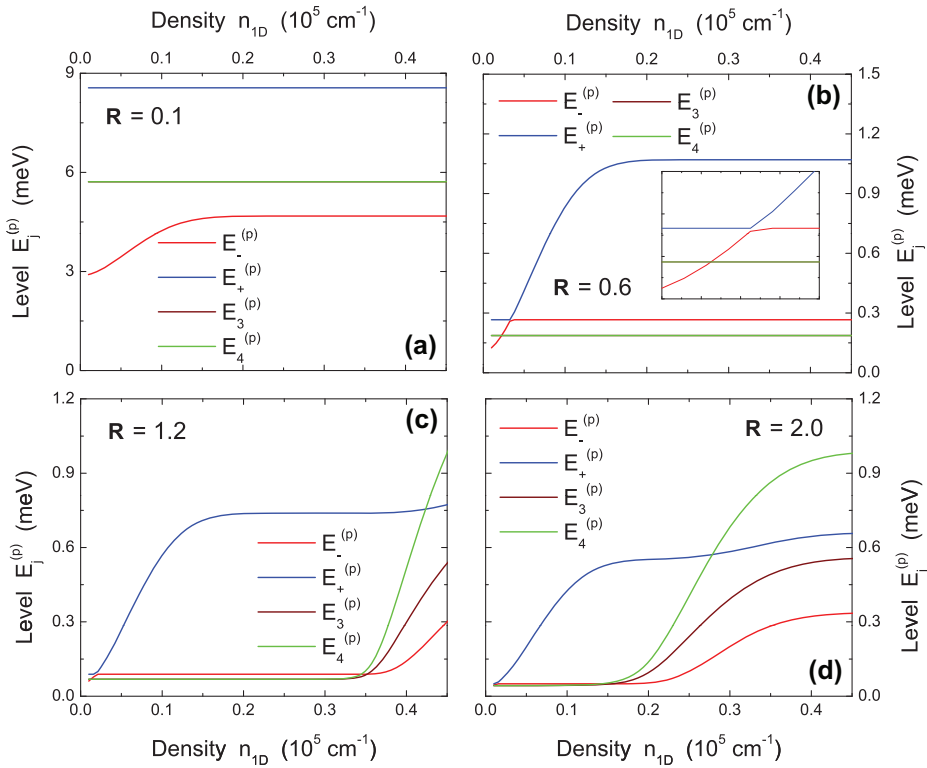
Figure 4. (Color online) Plots of cluster energy levels $E_j^{(p)}$ as a function of linear electron density n_{1D} with four different values of geometry ratio $\mathcal{R} = W_x/L_y$.

Note: Inset in 4(b) brings us a blow-out view for the anticrossing of energy levels $E_-^{(p)}$ and $E_+^{(p)}$.

level anticrossing observed in Figure 4(b). However, the new $4\,e^2/h$ conductance plateau is severely perturbed at higher densities by a sharp spike and followed by a deep dip to the lower $2\,e^2/h$ plateau as $\mathcal{R} = 1$ for intermediate confinement in 5(d).

Although the dimensionless Coulomb integrals do not depend on the linear electron density n_{1D}, the energy levels $E_j^{(p)} \sim \{u_{ij}\}$ for a two-electron cluster is proportional to the occupation factors (N_0 and N_1) in addition to these Coulomb integrals. Moreover, these occupation factors are determined by the chemical potential μ_n for noninteracting electrons through the Fermi function for fixed n_{1D}. On the other hand, the cluster chemical potential μ_p, determined by Equation (1), controls the behavior of cluster ballistic transport in the presence of a bias voltage V_b.

3.5. Conductance for weak confinement

We present in Figure 6 the change in the conductance plateau with increasing $\mathcal{R}$ in the weak confinement regime. When $\mathcal{R} \geq 1.6$, conductance plateaus for the noninteracting two-electron state are washed out in Figure 6(b)–(d) due to very small single-particle energy level separation compared to the thermal
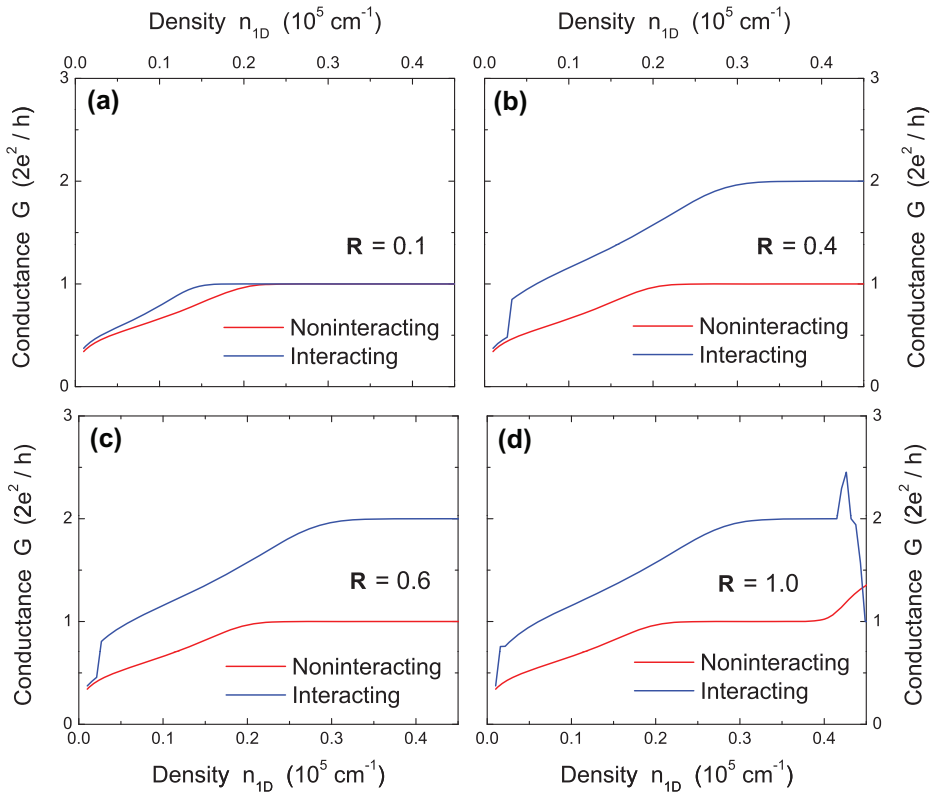
Figure 5. (Color online) Plots of conductance G as a function of linear electron density n_{1D} with four different values of geometry ratio $\mathcal{R}$ for both noninteracting and interacting cases.

energy $k_B T$. It is also evident that the incomplete $4\,e^2/h$ conductance plateau in Figure 6(a) for the interacting two-electron state is completely destroyed in this regime. However, the recovery of the single-particle-like $2\,e^2/h$ plateau, as displayed in Figure 5(a), is found in Figure 6. Additionally, the $2\,e^2/h$ plateau further expands and extends to lower and lower electron densities as $\mathcal{R}$ increases to 2.0 in Figure 6(d). This unique reoccurrence feature can be fully accounted for by the rising energy levels at higher densities due to the relatively enhanced Coulomb repulsion as shown in Figure 4(c) and (d).

As displayed in Figure 4, both $E_3^{(p)}$ and $E_4^{(p)}$ remain degenerate for all chosen values of n_{1D} as far as $\mathcal{R} < 1$ or alternatively for only small n_{1D} values as $\mathcal{R} > 1.2$. The level-crossing between $E_-^{(p)}$ and the degenerate levels $E_3^{(p)}$ and $E_4^{(p)}$ is the reason behind the upward jump of the conductance from 2 to $4\,e^2/h$, as can be seen from Figure 5. However, the degeneracy of the $E_3^{(p)}$ and $E_4^{(p)}$ levels may be lifted by an enhanced Coulomb repulsion for $\mathcal{R} > 1$ as well as for large values of n_{1D}. Consequently, the subsequent downward dip in the conductance from 4 to $2\,e^2/h$ is observed in Figure 6.

In order to acquire a complete picture of the quantum ballistic transport of interacting two-electron states passing through a quasi-1D conduction channel,
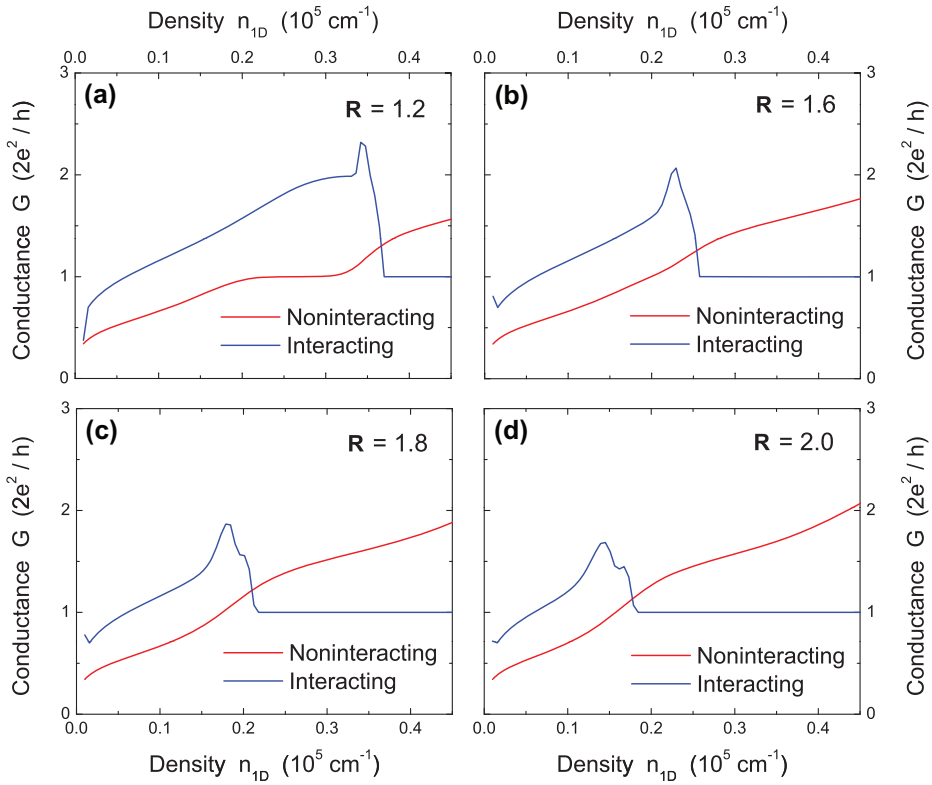
Figure 6. (Color online) Plots of conductance G as a function of linear electron density n_{1D} with another four different values of geometry ratio $\mathcal{R}$ for both noninteracting and interacting cases.
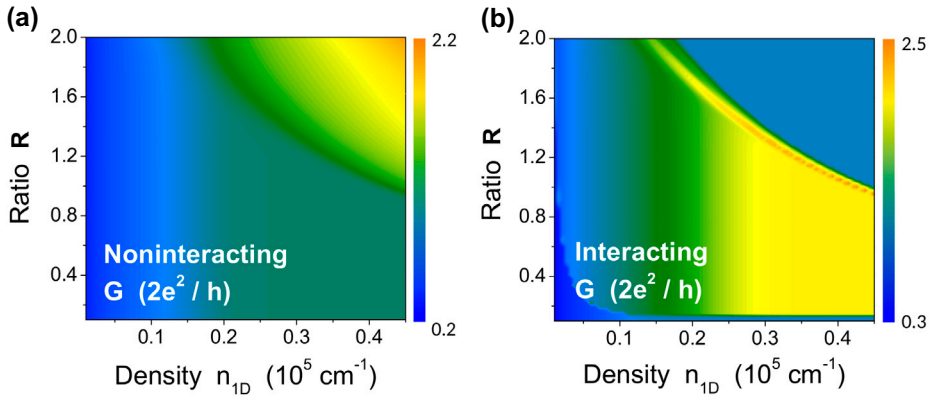

Figure 7. (Color online) Contour plots of conductance G as functions of both linear electron density n_{1D} and geometry ratio $\mathcal{R}$ for either noninteracting (left panel) or interacting (right panel) case.
Notes: As labeled by the color bars in this figure, the color scales (from blue up to orange) are [0.2, 2.2] (left) and [0.3, 2.5] (right), respectively.

we present the contour plots of electron conductance G as functions of $\mathcal{R}$ and n_{1D} in Figure 7 for both noninteracting and interacting two-electron states as a

direct comparison. By comparing Figure 7(a) with Figure 7(b), we find that the effect of the Coulomb coupling becomes most dominant in the upper right-hand corner of Figure 7(b) within a weak confinement regime and with a relatively high electron density at the same time. In this case, a gradually increasing conductance for noninteracting electrons is replaced by a $2\,e^2/h$ conductance plateau. This is due to the Coulomb repulsion in interacting two-electron states. In addition, another $4\,e^2/h$ conductance plateau shows up in the lower right-hand corner of Figure 7(b). This is separated by a spike in G from the upper right-hand corner. In this region, confinement is intermediate or strong but the electron density is high.

In our numerical results presented above, we limit the bias voltage V_b to a very small value (0.01 mV), where G becomes essentially independent of V_b. The increase of V_b can induce a 'hot-carrier' effect and reduce the ballistic conductance with increasing temperature, as presented in Figure 8, where the conductances G for both noninteracting [in Figure 8(a)] and interacting [in Figure 8(b)] with $V_b = 0.05$ mV are compared with each other. From Figure 7(a) and (b), we find G for noninteracting electrons has been changed qualitatively for different values of V_b, although G for electron clusters is only modified quantitatively. We further demonstrate such a bias dependent effect on G of electron clusters in Figure 8(c), where three different values of V_b are chosen for $n_{1D} = 0.3 \times 10^5$ cm^{-1}. As can be seen from Figure 8(c), the spike in G is significantly broadened and the plateau of G on both sides of the spike is reduced simultaneously with increasing V_b. This is similar to the hot-carrier effect with increased T.

We now turn our attention to the experimental aspects which are related to the preceding theoretical results. Two-terminal differential conductance measurements were performed with an excitation voltage of 10 μV at 73 Hz using the Oxford Instruments cryofree dilution refrigerator, where the device is estimated to have an electron temperature of around 70 mK.

In order to the test the samples, a top gated, split gate device provided additional confinement to the quasi-1D electrons. This allowed us to vary the confinement from being very strong (zero top gate) to very weak (very negative top gate voltage). In the present study, as shown in Figure 9, the top gate voltage, V_{tg}, is varied from -7.21 V (left) to -9.19 V (right) in steps of 90 mV.

Figure 9 shows a plot of the differential conductance in (a) for the device as a function of the split gate voltage V_{sg} for various values of the top gate voltage V_{tg}, as well as in (b) for the transconductance (dG/dV_{sg}) drawn from the data in (a). As can be seen from Figure 9(a), as the confinement is reduced, the $2\,e^2/h$ conductance plateau is weakened. If the confinement is further reduced, the $2\,e^2/h$ plateau disappears and is replaced by a direct jump in conductance to the (rounded) $4\,e^2/h$ plateau at both $V_{tg} = -8.47$ and -8.56 V (indicated by arrows). Eventually the first plateau at $2\,e^2/h$ is recovered on further reducing the confinement to $V_{tg} = -9.19$ V (right-most red curve). In comparison with
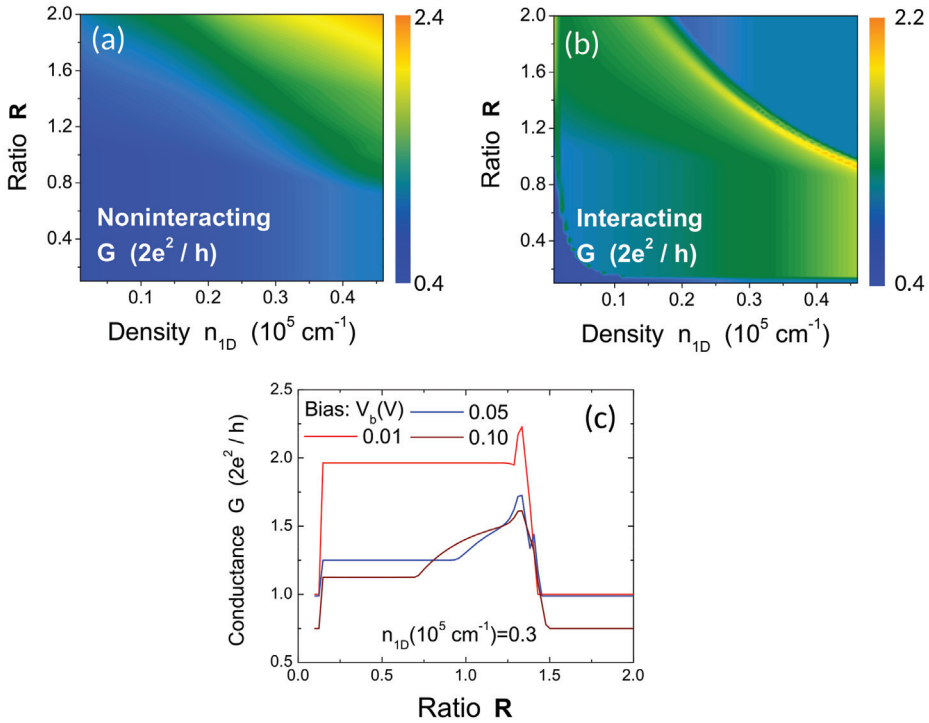
Figure 8. (Color online) Contour plots of G as functions of both linear electron density n_{1D} and geometry ratio $\mathcal{R}$ for either noninteracting (a) or interacting (b) case at $V_b = 0.05$ V, as well as the plot of G as a function of $\mathcal{R}$ (c) at $n_{1D} = 0.3 \times 10^5$ cm^{-2} for three different values of bias voltage V_b.

our calculated results presented in Figures 5 and 6, we find the sequence from the appearance of the $2\,e^2/h$ conductance plateau for small values of $\mathcal{R}$. We have obtained results for strong confinement as well as the $4\,e^2/h$ conductance plateau for intermediate confinement, and again the $2\,e^2/h$ conductance plateau in the weak-confinement regime which is preceded by a double-kink structure. In addition, from Figure 9(b) we know the crossing/anticrossing of the ground state and the first excited states depends on the confinement strength. Here, when V_{tg} is around -8.6 V, the ground state and the first excited states cross, leading to energy reversal such that previous excited state becomes the new ground state, and then, the previous ground state further moves up in the energy and anticrosses with the second excited state. This observation qualitatively agrees with the calculated results presented in Figure 2.

We would like to emphasize that the appearance/disappearance/reappearance of a conductance plateau has been qualitatively reproduced in our numerical calculations. This is displayed in Figure 3, although some nonmonotonic features in our reported results are not verified experimentally. We acknowledge that there is some nonmonotonic behavior in the results of our simulations, e.g. in Figures 3 and 6, preceding the onset of the first conductance plateau which is verified by the experimental data. However, apart from this, we do believe that we
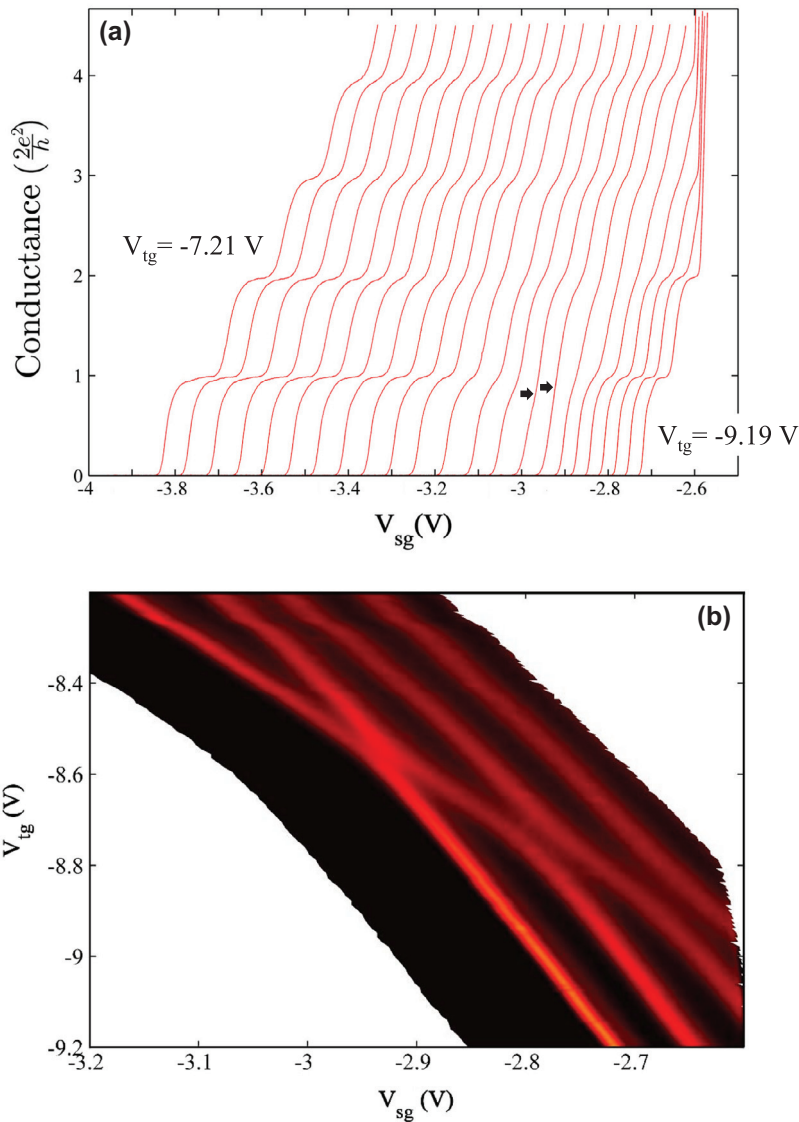
Figure 9. (Color online) Plot of measured differential conductance in (a) as functions of split gate voltage V_{sg} for various values of top gate voltage V_{tg}, and in (b) the transconductance (dG/dV_{sg}) plot of the data shown in (a).

Notes: The confinement in (a) is controlled by making the top gate negative so that left (right) of the plot is strong (weak) confinement, where a direct jump to $4\,e^2/h$ (indicated by arrows) occurs when the confinement is weakened using a top gated, split-gate device. In addition, the first trace in (a) on the left is taken at $V_{tg} = -7.21$ V and successive traces were plotted in steps of 90 mV until $V_{tg} = -9.19$ V.

have qualitatively reproduced a significant part of the experimentally observed recurrence of the first conductance plateau with increasing channel width. This is an aim of our review, and such an observation highlights the importance of the Coulomb interaction between electrons after appreciably suppressing the electron kinetic energy contribution as the channel confinement becomes very weak.

4. Concluding remarks

The ballistic conductance for a quasi-1D channel (quantum wire) has exhibited an interesting behavior as functions of the electron density as well as confinement. We demonstrated that electron–electron interaction plays a crucial role in our calculations in the weak confinement regime. Extensive calculations were carried out in regards the effects due to confinement on the conductance and its associated dependence on the interplay between level anticrossing and crossing in quantum transport of two interacting-electron clusters. As shown in our numerical results, depending on the confinement parameter, the conductance manifests the signature of single-particle or interacting two-electron state behavior. This dependence can be observed in the deviation of the conductance from $2\,e^2/h$ (single-particle) to $4\,e^2/h$ (interacting crossing state) and back to $2\,e^2/h$ (interacting anticrossing state) as a function of the width of the quantum wire. It is interesting to observe how many-body effects enter the calculation of the quantum ballistic conductance, where the center-of-mass velocity is not affected by the electron–electron interaction but the electron distribution is affected.

We conclude that the experimental observations qualitatively agree well with our theoretical calculations. Furthermore, such experimentally observed features for switching conductance plateau can be physically explained by the interchange of the ground between $E_-^{(p)}$ and the degenerate $E_3^{(p)}$ and $E_4^{(p)}$ and back to $E_-^{(p)}$, which is reflected as an upward jump from 2 to $4\,e^2/h$ and followed by another step jump from $4\,e^2/h$ back to $2\,e^2/h$ with increasing channel width. Additionally, we note that the Lüttinger-liquid behavior in a one-dimensional electronic system under the electrical-quantum limit is expected in the presence of an electron–electron interaction, where all electrons occupy the same lowest conduction subbband. However, in our system, four considered spin-dependent paired-electron states come from the combination of two electron orbital states associated with different conduction subbands. Therefore, the recovery of our system to the Lüttinger liquid should not occur here by going beyond this electrical-quantum limit. Thus, our system does not satisfy the major criteria of a Lüttinger liquid. On the other hand, in the electric-quantum limit, we do expect a full recovery of the Lüttinger-liquid behavior in our system as described by standard many-body theory. However, the effects of *tunneling of hybridized pairs of electrons through a one-dimensional channel* discussed in this paper will be lost completely in this limit.

Acknowledgements

Disclosure statement

No potential conflict of interest was reported by the authors.

References

[1] S. Kumar, K.J. Thomas, L.W. Smith, M. Pepper, G.L. Creeth, I. Farrer, D. Ritchie, G. Jones and J. Griffiths, Phys. Rev. B 90 (2014) p.201304(R).

[2] T.J. Thornton, M. Pepper, H. Ahmed, D. Andrews and G.J. Davies, Phys. Rev. Lett. 56 (1986) p.1198.

[3] D.A. Wharam, T.J. Thornton, R. Newbury, M. Pepper, H. Ahmed, J.E.F. Frost, D.G. Hasko, D.C. Peacock, D.A. Ritchie and G.A.C. Jones, J. Phys. C 21 (1988) p.L209.

[4] J. van Wees, H. van Houten, C.W.J. Beenakker, J.G. Williamson, L.P. Kouwenhoven, D. van der Marel and C.T. Foxon, Phys. Rev. Lett. 60 (1988) p.848.

[5] L. Maslov and M. Stone, Phys. Rev. B 52 (1995) p.R5539.

[6] J. Meyer and K. Matveev, J. Phys.: Condens. Matter 21 (2009) p.023203.

[7] H.J. Schulz, Phys. Rev. Lett. 71 (1993) p.1864.

[8] G. Piacente, I.V. Schweigert, J.J. Betouras and F.M. Peeters, Phys. Rev. B 69 (2004) p.045324.

[9] L.W. Smith, W.K. Hew, K.J. Thomas, M. Pepper, I. Farrer, D. Anderson, G.A.C. Jones and D.A. Ritchie, Phys. Rev. B 80 (2009) p.041306(R).

[10] D. Klironomos, J.S. Meyer, T. Hikihara and K.A. Matveev, Phys. Rev. B 76 (2007) p.075302.

[11] G. Smith, M. Pepper, R. Newbury, H. Ahmed, D.G. Hasko, D.C. Peacock, J.E.F. Frost, D.A. Ritchie, G.A.C. Jones and G. Hill, J. Phys. Condens. Matter 1 (1989) p.6763.

[12] P.J. Simpson, D.R. Mace, C.J.B. Ford, I. Zailer, M. Pepper, D.A. Ritchie, J.E.F. Frost, M.P. Grimshaw and G.A.C. Jones, Appl. Phys. Lett. 63 (1993) p.3191.

[13] K.J. Thomas, J.T. Nicholls, M.Y. Simmons, W.R. Tribe, A.G. Davies and M. Pepper, Phys. Rev. B 59 (1999) p.12252.

[14] I.M. Castleton, A.G. Davies, A.R. Hamilton, J.E.F. Frost, M.Y. Simmons, D.A. Ritchie and M. Pepper, Physica B 249–251 (1998) p.157.

[15] D.H. Huang, G. Gumbs, Y. Abranyos, M. Pepper and S. Kumar, AIP Adv. 5 (2015) p.117227.

[16] J. Faist, P. Guéret and H. Rothuizen, Phys. Rev. B 42 (1990) p.3217.

[17] G. Gumbs, A. Balassis, D.H. Huang, S. Ahmed and R. Brennan, J. Appl. Phys. 110 (2011) p.073709.

[18] L.W. Smith, K.J. Thomas, M. Pepper, D.A. Ritchie, I. Farrer, J.P. Griffiths and G.A.C. Jones, J. Phys.: Conf. Ser. 376 (2012) p.012018.

[19] J. Koch, M.E. Raikh and F. von Oppen, Phys. Rev. Lett. 96 (2006) p.056803.

[20] M. Leijnse, M.R. Wegewijs and M.H. Hettler, Phys. Rev. Lett. 103 (2009) p.156803.

[21] M. Wagner, U. Merkt and A.V. Chaplik, Phys. Rev. B. 45 (1991) p.1951.

[22] G.W. Bryant, Phys. Rev. Lett. 59 (1987) p.1140.

[23] S.K. Lyo and D.H. Huang, J. Phys.: Condens. Matt. 16 (2004) p.3379.

[24] G. Gumbs, D.H. Huang, M.D. Blumenthal, S.J. Wright, M. Pepper and Y. Abranyos, Semicond. Sci. Technol. 24 (2009) p.115001.

[25] S.K. Lyo and D.H. Huang, Phys. Rev. B 73 (2006) p.205336.

[26] G.R. Aizin, G. Gumbs and M. Pepper, Phys. Rev. B 58 (1998) p.10589.

[27] G. Gumbs, A. Balassis, D.H. Huang, S. Ahmed and R. Brennan, J. Appl. Phys. 110 (2011) p.073709.